Green Chemistry

# Spent tea leaves templated synthesis of highly active and durable cobalt-based trifunctional versatile electrocatalysts for hydrogen and oxygen evolution as well as oxygen reduction reactions

| Journal: | *Green Chemistry* |
|---|---|
| Manuscript ID | GC-ART-06-2020-002155.R2 |
| Article Type: | Paper |
| Date Submitted by the Author: | 25-Aug-2020 |
| Complete List of Authors: | Ahsan, Md Ariful; University of Texas at El Paso, Chemistry<br>Imam, Muhammad; University of Texas at El Paso, Chemistry<br>Puente Santiago, Alain Rafael; University of Texas at El Paso, College of Science<br>Rodriguez, Alejandro; University of Texas at El Paso<br>Alvarado-Tenorio, Bonifacio; Universidad Autonoma de Ciudad Juarez, Ciencias Quimico-Biologicas<br>Bernal, Ricardo; University of Texas at El Paso, Chemistry<br>Luque, Rafael; Universidad de Cordoba, Departamento de Quimica Organica<br>Noveron, Juan; University of Texas at El Paso, Chemistry |
| | |

**SCHOLARONE™**
Manuscripts

**Spent tea leaves templated synthesis of highly active and durable cobalt-based trifunctional versatile electrocatalysts for hydrogen and oxygen evolution as well as oxygen reduction reactions**

Md Ariful Ahsan,[a,b*] Muhammad A. Imam,[c] Alain R. Puente Santiago, [a*] Alejandro Rodriguez,[a] Bonifacio Alvarado-Tenorio,[d] Ricardo Bernal, [a] Rafael Luque,[e,f] and Juan C. Noveron [a,b*]

[a]*Department of Chemistry and Biochemistry, University of Texas at El Paso, 500 W. University Ave., El Paso, TX 79968, USA*

[b]*Nanosystems Engineering Research Center for Nanotechnology-Enabled Water Treatment, USA*

[c]*Department of Metallurgical and Materials Engineering, The University of Alabama, Tuscaloosa, AL 35487, USA.*

[d]*Universidad Autonoma de Ciudad Juarez, Ciudad Juarez, Mexico.*

[e]*Departmento de Quimica Organica, Facultad de Ciencias, Universidad de Cordoba, Campus de Rabanales, Edificio Marie Curie (C-3), Ctra Nnal IV-A, Km 396, E14014 Cordoba, Spain*

[f]*Peoples Friendship University of Russia (RUDN University), 6 Miklukho Maklaya str., 117198, Moscow, Russia*

*Corresponding Author: arpuentesan@utep.edu, mahsan2@miners.utep.edu, jcnoveron@utep.edu*

## Abstract

The rational design of high-performance trifunctional catalysts for oxygen reduction, oxygen and hydrogen evolution reactions is of vital importance for the implementation of green energy conversion technologies. Herein, trifunctional electrocatalysts comprising cobalt nanoparticles uniformly embedded in porous carbon networks were fabricated using spent tea leaves (STL) template via a one-step carbothermal-reduction strategy at different temperatures. STL played a dual synthetic function to construct the nanocatalysts acting as efficient scavengers to trap cobalt cations via electrostatic interactions and as carbon sources to generate the porous carbon matrix. Full characterization of the as-synthesized materials revealed the crucial role of temperature on the crystallinity, surface area, number of surface defects and interfacial charge distribution properties. Furthermore, the trifunctional catalytic activity of the nanoparticles can be nicely tuned by varying the carbonization temperature. Co@PC-7 displayed a superior trifunctional catalytic activity rendering an excellent performance for hydrogen production with an overpotential potential of 153 mV (vs RHE) to achieve 10 mA·cm$^{-2}$, and an impressive bifunctional catalytic performance for the overall oxygen activity with an ultralow potential difference of OER and ORR ($\Delta E = \eta_{10} - E_{1/2}$) of 0.69 V, which is one of the lowest values reported in the literature for transition metal nanocatalysts. The remarkable performance of Co@PC-7 is mainly ascribed to its unique structural properties, which give rise to highly desirable charge distributions at the metal/carbon electrochemical interfaces to perform efficient trifunctional water splitting electrocatalysis.

**Keywords:** Co NPs; Spent Tea Leaves; Green synthesis; Hydrogen evolution reaction; Oxygen evolution reaction; Oxygen reduction reaction.

## 1. Introduction

Sustainable routes to design energy-related nanomaterials with multifunctional catalytic functions are paving the way for the next generation of green electrocatalysts and, in turn, opening horizons for the development of innovative clean energy technologies.[1-4] These synthetic routes constitute powerful tools to synthesize several competitive energy conversion materials avoiding both harmful reactives and high energy-consumption methodologies.[5, 6] Resulting nanomaterials usually exhibit low-cost, facile manufacture, high abundance in nature, easy scale-up and ultra-efficient electrocatalytic behavior.[7, 8] Besides, they have recently started to be highly competitive alternatives to traditional precious catalysts ($Pt/RuO_2/IrO_2$) in a myriad of catalytic reactions including HER, OER and ORR.[9] [10] Among most attractive nanostructures, transition metal nanoparticles (TMNPs) have gained increasing interest due to their desirable structural properties for the development of high-performance electrocatalysts.[11-14] Nevertheless, the catalytic performance of bare TMNPs is rather unstable in specific experimental conditions such as strong alkaline environments and large overpotentials due to both their higher surface to volume ratio and high surface energy, thus hindering their applications in electrocatalysis.[14-16] Consequently, the wrapping of the air-sensitive metal 3d TMs with a protective material could be an effective strategy to solve the aforementioned drawbacks. In this sense, several protective materials such as porous carbon, $Al_2O_3$, $SiO_2$ have been using for this purpose.[15, 17-19] Recently, the encapsulation of 3d TMs in different classes of carbon matrices have appeared as an effective concept to achieve catalytic nanosystems with superior HER, ORR and OER activities.[20, 21] The carbon network protects the metallic cores from harsh conditions and avoid its phase transformation, thus boosting several times the electrochemical stability and durability of the resulting carbon-coated TM nanocatalysts. This alternative has been effective in tuning the electrocatalytic rates of TMNPs by

tailoring the structure of the carbon frameworks such as edges, heteroatom doping, defects and thickness.[20, 22] Particularly, the design of carbon encapsulated TMNPs heterostructures with numerous defects in the carbon matrix have greatly enhanced the bifunctional catalytic activity of the single components due to the interfacial electron gathering processes in the defective carbon moieties at the metal/carbon electrochemical interfaces, demonstrating that the control of the number of carbon surface defects can finely tuned the interfacial charge distribution and, in turn, the catalytic performance.[23]

The tea leaves are one of the most popular drinks in the world and almost 18 to 20 billion cups of tea are consumed every day all over the world.[24] Therefore, plenty of spent tea leaves from industry and household are always dumped into the environment that doesn't show any economical importance, rather it accumulates too much waste in our surroundings. In this regard, the valorization of this waste is highly desirable. Herein, we report a simple, green and effective carbothermal reduction strategy through directly carbonizing a mixture of spent tea leaves and cobalt nitrate salt at different temperatures (600/700/800 °C) for one-pot synthesis of Co@PC electrocatalysts, in which Co NPs are highly dispersed on the instantaneously produced porous carbon matrix (PC). Despite the energy-consumption methodology, this work paves the way towards the valorization of beverage wastes via an inexpensive and simple strategy to build very efficient carbon-encapsulated trifunctional nanocatalytic systems. As a result, the huge amount of tea waste can be efficiently recycled and converted into valuable materials, while cleaning the environment at the same time. The entire synthesis process avoids the use of reducing agents and surfactants, thereby reducing environmental pollution and saving cost. The structural and catalytic properties of Co@PC electrocatalysts for different reactions such as hydrogen evolution, oxygen evolution and oxygen reduction reactions can be finely tuned varying the carbonization

temperature. Additionally, the high number of surface defects provides Co@PC-7 with unique interfacial properties to enhance the accumulation of electrons at the carbonaceous matrix, thus increasing both the number of catalytic active sites and the trifunctional OER/ORR/HER performance. This work features several green credentials including the non-use of hazardous or toxic chemicals, the minimization of both resources and energy required to generate the catalysts, atoms economy due to the multifunctional catalytic functions of the synthesized nanocatalysts and the use of waste feedstocks as starting material for catalyst design.

## 2. Experimental Section

### 2.1 Chemicals and Materials

Spent tea leaves were collected from a local store in El Paso, Texas, USA. Sulfuric acid, potassium hydroxide, cobalt nitrate hexahydrate, Nafion solution, $RuO_2$, commercial Pt/C (40wt%) and methanol were obtained from Fisher Scientific and Sigma-Aldrich. All chemicals were used without any further purification and the deionized water (DI) was used in all experiments.

### 2.2 Synthesis of cobalt-based electrocatalysts

Spent tea leaves (STL) were firstly washed with DI water to remove any dirt and then boiled for 1 h to remove tannin, caffeine or any other coloring materials.[25] STL were then vacuum filtered and dried in an oven for 12 h at 70 °C. In a typical synthesis procedure of electrocatalysts, 3 g of cobalt salt was added into a 50 mL beaker and dissolved in 20 mL of DI water. Afterward, 3 g of dried STL was poured into the metal salt solution followed by a tip sonication for 1 h so that the metal ions ($Co^{2+}$) can be well dispersed all over the surface of STL. This bi-mixture was then heated in a hot plate to ca. 100 °C to remove all the water. The dried bi-mixture of STL and cobalt

salt was then kept in a crucible boat and calcined at different temperatures, viz. 600, 700 and 800

°C in an argon environment for 3 h at a heating rate of 5 °C/min. Once the sample was cooled down

to room temperature, it was taken out and saved in a glass vial for further use. The samples were

denoted as Co@PC-6, Co@PC-7 and Co@PC-8 depending on their carbonization temperature (for

example: 6, 7 and 8 define the samples that were prepared at 600, 700 and 800 °C, respectively).

As controls, porous carbon (PC) and cobalt nanoparticles (Co NPs) were also prepared following

the same procedure with only spent tea leaves or cobalt salt used in the synthesis process.

## 2.3 Electrochemical measurements

HER, OER and ORR experiments were performed on an electrochemical workstation

(model: CHI 760E). All experimental data were obtained using a three-electrode system that

consists of a glassy carbon, graphite rod and Ag/AgCl electrode as the working, counter and

reference electrode, respectively. To prepare the electrocatalyst ink, 4 mg of cobalt sample was

added into a solution containing 970 µL of methanol and 30 µL of 5% Nafion. Afterward, the

solution was ultrasonicated for 30 min to form a homogenous mixture. Then, 10 µL of catalyst ink

was loaded uniformly on the glassy carbon electrode. The linear sweep voltammetry (LSV)

measurements were performed in 0.5 M $H_2SO_4$ solution for the HER process and in 0.1 M KOH

solution for the OER and ORR processes at a scan rate of 2 mV·s$^{-1}$. The obtained potentials were

converted into the reversible hydrogen electrode (RHE) based on the following Nernst equation.[26]

$$E_{RHE} = E_{Ag/AgCl} + 0.059 \text{ pH} + 0.197 \qquad (1)$$

Tafel plots were obtained from LSV measurements and the analysis was performed according to

the equation:[26]

$$\eta = a + b \log j \qquad (2)$$

where b is the Tafel slope, $\eta$ is the overpotential and j is the current density.

The electrochemical active surface area (ECSA) of the electrocatalysts was obtained by evaluating the electrochemical double-layer capacitance ($C_{dl}$) using cyclic voltammetry (CV) measurements at different scan rates viz. 2, 5, 10, 15 and 20 mV·s$^{-1}$. Then, the difference between anodic and cathodic current densities against the scan rate was plotted to find the slope as the slope is defined as $C_{dl}$. Finally, the ECSA was calculated by using the following equation[27, 28]

$$ECSA = C_{dl}/C_s \qquad (3)$$

Where $C_s$ is the specific capacitance of the catalysts. The roughness factors (RF) were also calculated using the following equation.

$$RF = (ECSA) / (geometric\ area\ of\ the\ electrode) \qquad (4)$$

A glassy carbon disc of 5 mm in diameter (Pine Instruments Company) was used as the working electrode for the rotating disc electrode (RDE) measurements. All electrochemical experiments were performed employing a potential range from 0.00 to −0.75 V vs Ag/AgCl at a scan rate of 10 mV/s. All potentials were referenced to RHE. Kinetic parameters such as kinetic current density ($J_k$) and electron transfer number (n) were estimated according to Koutecky-Levich (K-L) equations.[26]

$$\frac{1}{J} = \frac{1}{J_L} + \frac{1}{J_K} = \frac{1}{B\omega^{1/2}} + \frac{1}{J_K} \qquad (5)$$

$$B = 0.20\ nFC_0D_0^{2/3}v^{-1/6} \qquad (6)$$

where J is the measured current density, $J_L$ and $J_k$ are the diffusion and kinetic current density, F is the Faraday constant, $\omega$ is the electrode rotation rate, $n$ is the overall number of electrons transferred for the oxygen reduction, $C_0$ is the bulk concentration of $O_2$ ($1.2 \times 10^{-6}$ mol·cm$^{-3}$), $D_0$

is the diffusion coefficient of $O_2$ ($1.9 \times 10^{-5}$ cm$^2$·s$^{-1}$), and $\upsilon$ is the kinetic viscosity of the electrolyte (0.01 cm$^2$ s$^{-1}$). To calculate the faradaic efficiency (FE) for HER and OER of the best electrocatalyst (Co@PC-7), chronoamperometry measurements at a constant potential (E = $-150$ mV) for five specific times were performed and the volume of the generated hydrogen and oxygen gases were calculated using a water displacement method.[29]

## 3. Results and discussion

### 3.1 Synthesis and characterization of the electrocatalysts

The synthesis of Co@PC electrocatalysts involved a simple green and sustainable adsorption process of the metal ions onto the spent tea leaves followed by a one-step carbonization process at 600,700 and 800°C, illustrated in **Fig. 1A.** Initially, spent tea leaves were mixed with cobalt salt solution and subsequently, metal ions (Co$^{2+}$) were adsorbed on the surface of the spent tea leaves due to electrostatic interactions between positively charged cobalt ions and negatively charged functional groups in spent tea leaves (cellulose and lignin). Metal ions-loaded spent tea leaves can serve as both metal precursor and carbon source for the preparation of Co@PC electrocatalysts. When metal ions-loaded spent tea leaves were carbonized under an argon atmosphere, spent tea leaves gradually carbonized to form a porous carbon (PC) matrix and at the same time, the cobalt ions were getting reduced to form metallic cobalt nanoparticles by the PC via a carbothermal reduction strategy. Afterward, the cobalt nanoparticles were loaded on the PC matrix to yield the desired electrocatalysts (Co@PC).

The spent tea leaves (STL) were firstly characterized using FTIR, XPS, SEM and EDS to investigate the chemical composition of STL. **Fig. S2A** illustrates the FTIR spectra of STL and it

shows a broad peak at around 3500-3200 cm$^{-1}$ indicating that the structure of STL is rich in OH groups. The other two peaks at around 1635 and 1520 cm$^{-1}$ correspond to the asymmetric stretching vibrations of C=O and aromatic compound groups. The peaks observed at around 2923-2850 cm$^{-1}$ correspond to the aliphatic C-H groups. The other prominent band at 1046 cm$^{-1}$ is due to the C-O stretching. **Fig. S2B** represents the XPS spectra of STL and it shows the presence of carbon and oxygen only. **Fig. S2C** shows the morphological analysis of STL by SEM and it is clear from this figure that the STL is mainly composed of micron-size particles. The EDS analysis of STL was further performed and it also confirmed the presence of carbon (67.69%) and oxygen (32.31%), as seen in **Fig. S2D**.

The crystal structures of as-synthesized electrocatalysts were firstly studied by X-ray diffraction (XRD). The diffraction pattern of Co@PC-6 displayed three characteristic peaks at around 44.04, 51.40 and 75.71°, that is characteristic of the (111), (200) and (220) planes of the face-centered cubic (FCC) metallic cobalt (JCPDS No.15-0806), respectively **(Fig. 1B)**.[28, 30] The other two samples (Co@PC-7 and Co@PC-8) also showed similar characteristic diffraction peaks with a slight shift. We have then closely investigated the peaks correspond to the (111) plane ($2\theta_{111}$ = 44.04, 44.27 and 44.19 for Co@PC-6, Co@PC-7 and Co@PC-8, respectively) using Bragg's law and crystal geometry equation of FCC crystal structure ($d_{hkl} = \lambda / 2Sin(\theta_{hkl}) = [ (h^2 + K^2 + l^2) / a^2]^{-1/2}$) to investigate any change on the crystalline structure due to different carbonization temperatures (results presented in **Table S1)**. Interestingly, the diffraction peak intensity of the electrocatalysts were markedly increased at higher carbonization temperatures (**Fig. 1B**), indicating that the reaction temperature is playing a key role on the overall crystallinity of the electrocatalysts.[31] Moreover, any extra diffraction peaks corresponding to the cobalt oxide ware not detected in the XRD pattern confirming the existence of pure metallic cobalt phase in Co@PC samples. Compared to the XRD peaks of the metallic cobalt that appear with higher intensity, the

diffraction peaks of porous carbon are hardly visible. To get insights on the structural properties of the carbon matrix of the electrocatalysts, we have performed Raman spectroscopic analysis of all Co@PC electrocatalysts and the results are presented in **Fig. 1C**. Two characteristic Raman bands of porous carbon appeared at ~ 1350 and 1590 cm$^{-1}$, which correspond to D and G bands, respectively.[32] D band is usually related to the disordered sp$^3$ type carbon (disorder and defects-induced features), whereas G band corresponds to the graphite sp$^2$ type carbon.[33, 34] The intensity ratio of D and G bands that are also referred to the ratio of amorphous to graphitic carbon ($I_D/I_G$) were calculated and found to be 0.99, 1.06 and 0.87 for Co@PC-6, Co@PC-7 and Co@PC-8 electrocatalysts, respectively. The $I_D/I_G$ value increases with increasing reaction temperature from 600 to 700 °C as more edges are exposed during the pore evolution process.[35] The obtained higher $I_D/I_G$ value for Co@PC-7 demonstrates the abundance of defective sites as well as non-graphitic or disordered carbon in Co@PC-7, which can substantially boost its electrocatalytic performance.[28] The defects or lattice edges on the surfaces of PC constitute potential catalytically accessible active sites that could improve the electrochemical activity of Co@PC-7 hybrid composite.
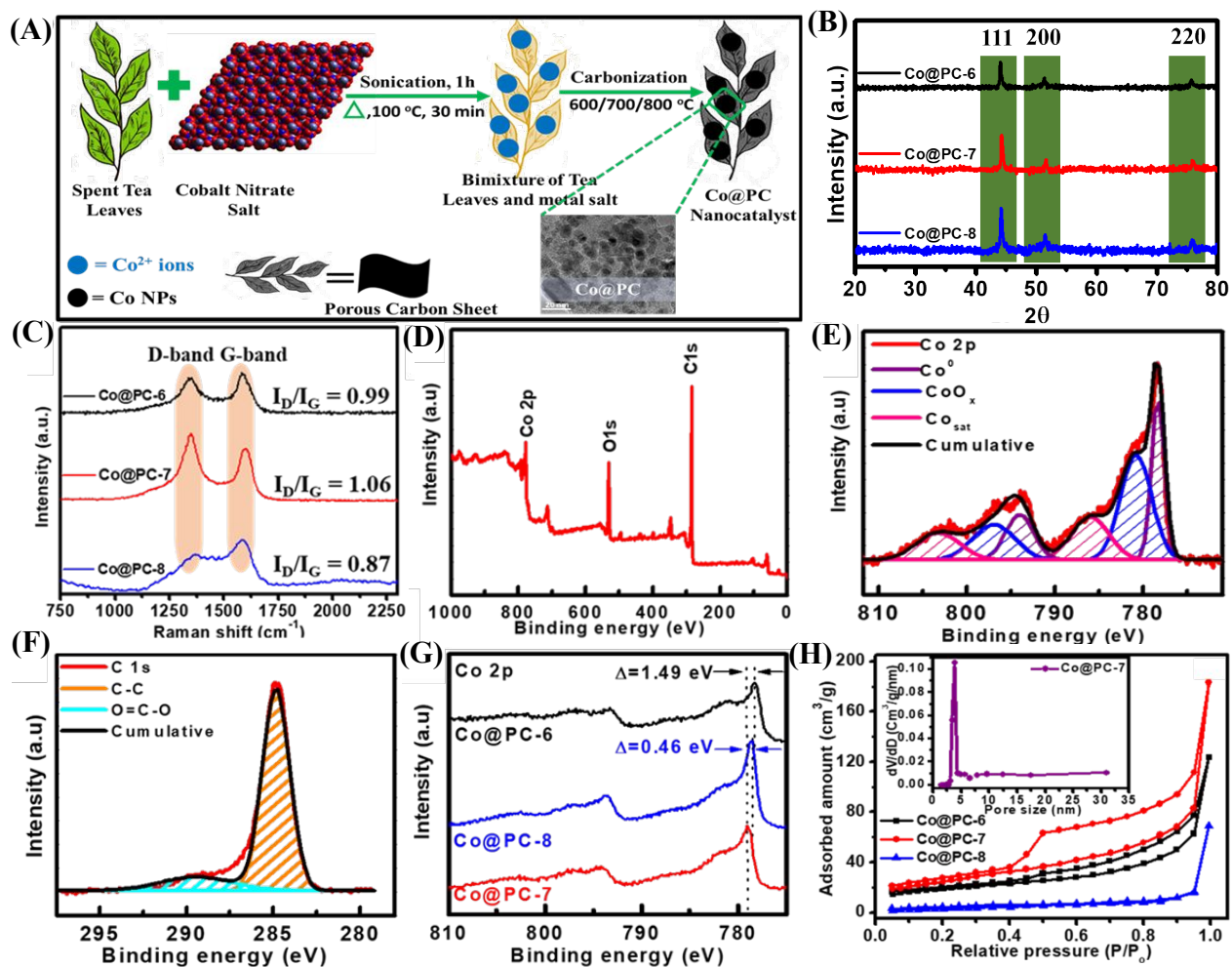
**Fig. 1.** (A) Schematic representation of the Co@PC electrocatalyst synthesis process; (B-C) XRD and Raman analysis of the Co@PC-6, Co@PC-7 and Co@PC-8 electrocatalysts, respectively; (D) XPS survey of the Co@PC-7 electrocatalyst and the corresponding high-resolution XPS spectra of (E) Co 2p, (F) C 1s and (G) comparison of the Co 2p bands in the Co@PC-6, Co@PC-7 and Co@PC-8 electrocatalysts; (H) $N_2$ sorption isotherm curves of the Co@PC-6, Co@PC-7 and Co@PC-8 electrocatalysts (inset: BJH pore size distribution of Co@PC-7).

To understand the graphitization process, Thermogravimetric analysis (TGA) was also performed for Co@PC electrocatalysts and illustrated in **Fig. S3**. The more metallic Co content was observed with increasing the processing carbonization temperature indicating the burnout of

the amorphous carbon and the increase in net graphitic carbon for Co@PC samples, in good agreement with previous literature.[36] The weight loss around 250 °C to 700 °C could be attributed to the destruction of the amorphous carbon and the deoxygenation of the oxygenated functional groups that are present on the nanocatalyst's surface, such as CO and OH in the forms of $CO_2$, CO and $H_2O$.[37] TGA analysis enabled the observation of three stages of carbonization process including initiation, intermediate and final stage. The more stable Co@PC was found at 800°C, indicating the final stage of the carbonization process. 700°C refers to the intermediate stage of carbonization process that contains more lattice edges or defects in disordered graphitic carbon in the process of transitioning from amorphous to graphitic carbon as confirmed by $I_D/I_G$ ratio of Raman spectra (**Fig. 1C**).

The elemental composition and surface analysis of Co@PC-7 electrocatalyst was investigated using X-ray photoelectron spectroscopy (XPS). As shown in **Fig. 1D**, XPS survey spectrum of Co@PC-7 shows the coexistence of C, O and Co elements in the sample. A high-resolution Co spectrum was recorded to examine the chemical states of Co active components. Co 2p spectrum was used in this current study for further analysis (**Fig. 1E**). As seen, Co 2p core level is mainly comprising of two spin-orbit components of Co $2p_{3/2}$ (eV) and Co $2p_{1/2}$ (eV). The Co $2p_{3/2}$ and Co $2p_{1/2}$ high-resolution spectra were fitted into three components corresponding to Co (0), Co (II) and satellites.[38, 39] The first peak was found to be at ca.778.2 eV, attributed to cobalt in a zerovalent state.[36] The second peak was found to be at ca.780.0 eV, ascribed to cobalt in a 2+ valent state, usually corresponding to cobalt oxide (CoO). This might happen due to the air exposure of the nanoparticles that could lead to forming a thin shell of CoO since Co (0) is sensitive to aerobic atmosphere.[40] However, the dominant existence of Co (0) in XPS measurements demonstrates that metallic Co NPs are mainly present on Co@PC-7, which essentially enhances

the electronic conductivity of the composites. To obtain additional insights into oxygen-containing species on the electrocatalyst surface, C 1s and O 1s spectra were subsequently recorded. As seen in **Fig. 1F**, the deconvolution of C 1s spectrum displays mainly two types of C species: C–C (284.7 eV) and –O–C=O (289.3 eV), which indicates that carbon atoms are connected to oxygen heteroatoms.[41] The high-resolution O 1s spectrum was fitted into three components/peaks with binding energies of about 529.8, 531.7 and 533.3 eV that are attributed to $O^{2-}$, bridging hydroxyls (C–OH) and physically absorbed water ($H_2O$), respectively (**Fig. S4**).[42, 43] These findings indicate the presence of a large content of oxygen-containing species on the electrocatalyst's surface that enables good dispersion of cobalt nanoparticles on the porous carbon matrix. Also, Co 2p spectra of Co@PC-8, Co@PC-7 and Co@PC-6 were compared (**Fig. 1G**). It is of great importance to highlight that the peaks of Co@PC-7 at 779 eV were slightly shifted to larger BE values as compared to Co@PC-6 and Co@PC-8. These results demonstrated that electron transfer from Co metal cores to the surrounding carbon network is more effective in Co@PC-7 nanoparticles, which lead to an electron gathering phenomenon at the surface defects of the metal/carbon interfaces, which can improve electron mobility and, in turn, electrocatalytic activity.[23] Nitrogen adsorption and desorption experiments were further performed to analyze the surface area and porosity of the prepared Co@PC nanocatalysts (**Fig. 1H**). Among all the Co@PC samples, only the $N_2$ adsorption and desorption isotherm of Co@PC-7 displays a typical type IV isotherm with a higher BET surface area of 128.20 $m^2 g^{-1}$. The characteristic hysteresis loop that is only observed for Co@PC-7 in the range of 0.4-0.8 ($P/P_0$), demonstrates the existence of a mesoporous structure and this information could also be verified from the pore size distribution plot as seen in **Fig. 1H (inset)** with an average pore size value of 3.85 nm.[7]
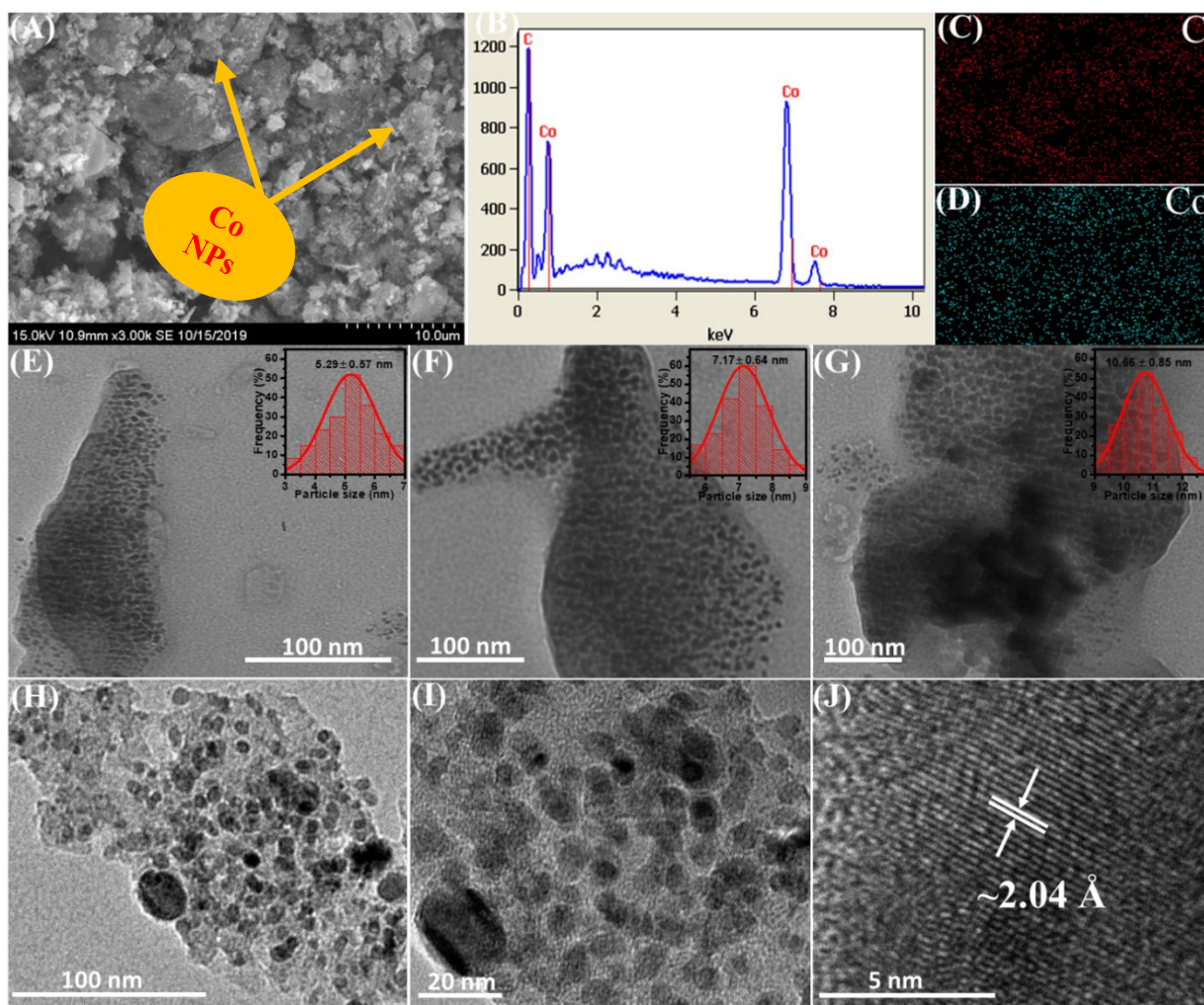
**Fig. 2** (A) SEM image, (B) EDS analysis and (C-D) elemental color mapping of the Co@PC-7 electrocatalyst; (E-G) TEM images of the Co@PC-6, Co@PC-7 and Co@PC-8 electrocatalysts, respectively; (H-J) HRTEM images of the Co@PC-7 electrocatalyst at different magnifications.

Surface morphology and elemental composition of Co@PC electrocatalysts were studied using SEM-EDS, with results presented in **Fig. 2(A-B)** and **Fig. S5(A, E)**. As shown in SEM images, cobalt nanoparticles are well dispersed throughout the carbon matrix. Furthermore, EDS analysis revealed that the electrocatalysts were mainly composed of carbon and cobalt, whereas samples prepared at higher carbonization temperatures displayed a higher cobalt content, in

agreement with TGA results, as seen in **Fig. 2B** and **Fig. S5(B, F)**. Moreover, the elemental color

mapping images also clearly indicate the coexistence and distribution of carbon and cobalt

elements in Co@PC electrocatalysts (**Fig. 2(C-D), Fig. S5(C-D)** and **Fig. S5(G-H)**). It also

confirms the good uniformity of Co and C elements in Co@PC, where Co NPs are well dispersed

in the porous carbon networks. Transmission electron microscopy (TEM) was also employed to

investigate the morphology and structure of as-synthesized electrocatalysts (**Fig. 2(E-G))**. Co NPs

were well dispersed into the porous carbon matrix in all cases. The average size from TEM analysis

was determined to be 5.29 ± 0.57, 7.17 ± 0.64 and 10.66 ± 0.85 for Co@PC-6, Co@PC-7 and

Co@PC-8 electrocatalysts, respectively. It was observed that the particle size of the nanoparticles

is increased with increasing carbonization temperature, which is ascribed to the metal sintering

and particle agglomeration effects. The uniformly embedded cobalt nanoparticles within the

carbon matrix could efficiently prevent further aggregation and oxidation processes. It also might

lead to a faster electron transport between the nanoparticles and carbon matrix, which, in turn, will

favorably affect their catalytic activities.[44] Transition metal/oxide phases within the graphitized

carbon matrix were previously reported to be conductive and greatly boost the electrocatalytic

activity of electrocatalysts.[38, 45] In this sense, it can be predicted that our developed Co@PC

electrocatalysts might follow a similar trend because of the interaction between the carbon matrix

and small-sized cobalt nanoparticles. High-resolution TEM (HRTEM) was further performed to

confirm the crystal structure of the cobalt nanoparticles. **Fig. 2(H-J)** depicts HRTEM images of

Co@PC-7 electrocatalyst at different magnifications, with results again confirming the ultrafine

distribution of Co NPs in the porous carbon matrix. As displayed in HRTEM images of Co@PC-

7, the well-defined crystal fringes with a lattice distance or d-spacing of about 2.04 A° can be well

indexed within the (111) crystal planes of a metallic cobalt phase (**Fig. 2J**).[28] This result is also in

good agreement with the d spacing value obtained for the (111) plane of Co NPs from XRD analysis.

## 3.2 Electrochemical hydrogen generation

The electrocatalytic performance of Co@PC-7 for HER was firstly evaluated in a 0.5 M $H_2SO_4$ solution with a three-electrode system. For comparison, similar experiments were also performed for Pt/C, Co@PC-6 and Co@PC-8 electrocatalysts. **Fig. 3A** represents the obtained LSV polarization curves for Pt/C, Co@PC-6, Co@PC-7 and Co@PC-8. Co@PC-7 displayed the highest HER performance with a very small onset potential of ca. -48 mV and an overpotential ($\eta_{10}$) of ca.153 mV to obtain a current density of 10 mA·cm$^{-2}$ that outperformed by far activities of Co@PC-6 ($\eta_{10}$ = 576 mV) and Co@PC-8 ($\eta_{10}$ = 395 mV) (**Table S2**). The obtained results indicated that the carbonization temperature plays a vital role in overall HER activity. In this sense, the electrocatalyst prepared at 700 °C exhibited a superior HER performance. It is noteworthy to mention that Co@PC-7 also displayed a comparatively higher performance to many other recently reported HER electrocatalysts, thus exhibiting one of the top-tier onset potential values among monometallic and bimetallic HER catalysts (**Table S6**).

To gain a better understanding on the HER kinetics, Tafel plots were obtained from the corresponding LSV polarization curves. The slopes derived from Tafel plots usually play a key role in investigating the rate-determining steps of the electrocatalytic HER process. Tafel slopes were found to be 240, 81 and 135 mV·dec$^{-1}$ for Co@PC-6, Co@PC-7 and Co@PC-8 electrocatalysts, respectively (**Fig. 3B**). Lower Tafel slope display better HER kinetics. Therefore, according to the obtained results, Co@PC-7 exhibited enhanced HER kinetics.
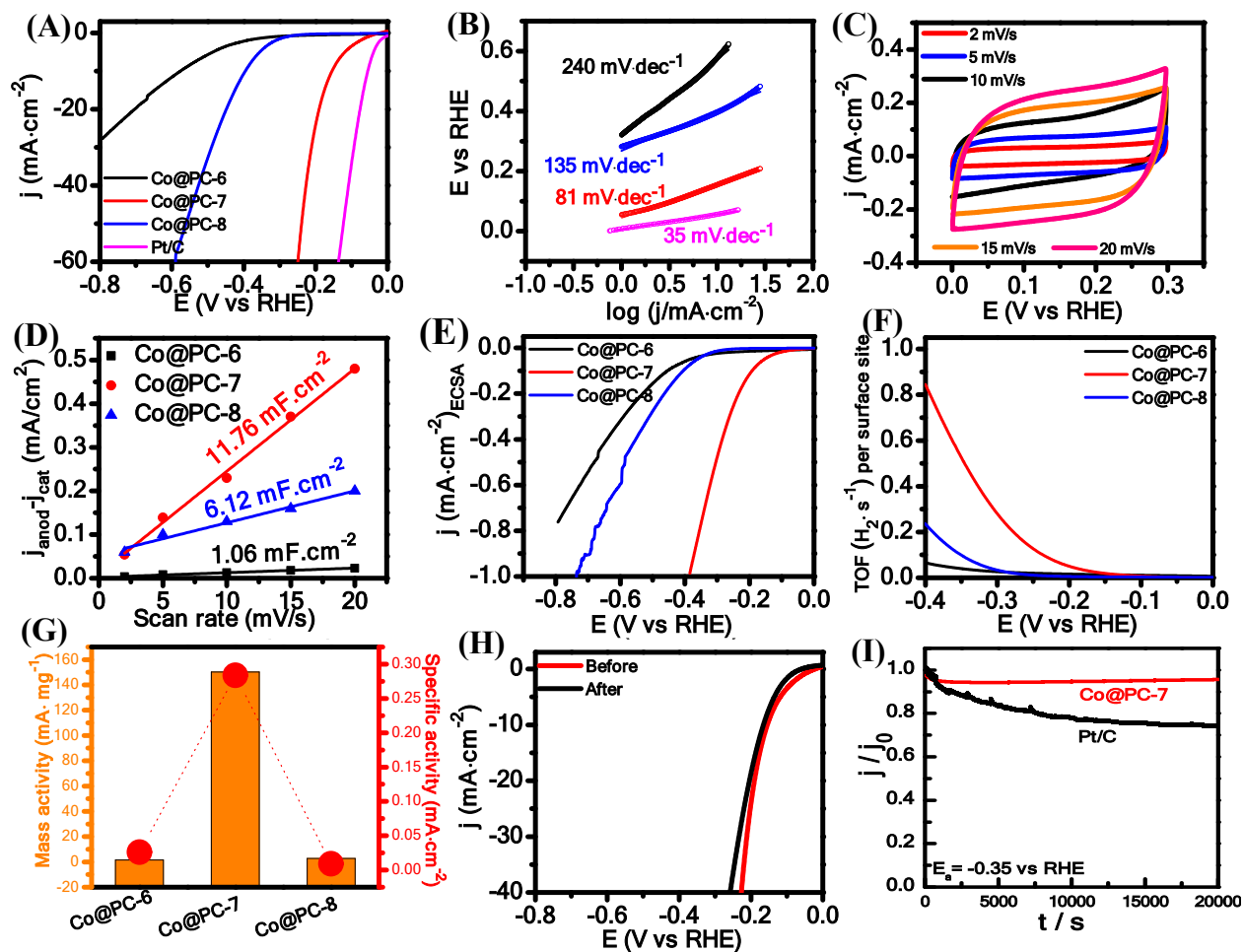
**Fig. 3** (A) LSVs for HER and (B) the corresponding Tafel plots of Co@PC-6, Co@PC-7, Co@PC-8 and commercial Pt/C in 0.5 M $H_2SO_4$ solution at 2 mV·s$^{-1}$. (C) electrochemical capacitance measurements to determine the ECSA of Co@PC-7. (D) plots of the difference of anodic and cathodic current densities against the scan rate for Co@PC-6, Co@PC-7 and Co@PC-8 electrocatalysts. (E) HER polarization curves normalized by ECSA; (F) the average turn-over frequencies (TOF$_{avg}$) of the nanocatalysts displayed in (A) per surface site; (G) mass and specific activity values of Co@PC-6, Co@PC-7 and Co@PC-8 catalysts; (H) LSV at one cycle (red line) and after 1000 cycles (black line) of Co@PC-7 catalyst in $N_2$ saturated 0.5 M $H_2SO_4$ solution at 2 mV·s$^{-1}$  (I) I-t curves of Co@PC-7 electrocatalyst and its comparison with commercial Pt/C at -0.35 V vs RHE.

In an aqueous electrolyte, $H^+$ ions gained electrons to generate hydrogen (H) atoms, subsequently adsorbed on the working electrode's surface (Volmer reaction: $H_3O^+ + e^- \rightarrow H_{ads}$), either followed by a Heyrovsky or electrochemical desorption step ($H_{ads} + H_3O^+ + e^- \rightarrow H_2$) or a Tafel or chemical desorption step ($H_{ads} + H_{ads} \rightarrow H_2$) to generate molecular hydrogen ($H_2$).[7] The theoretical Tafel slope values of Tafel, Heyrovsky and Volmer reactions were 30, 40 and 120 $mV \cdot dec^{-1}$, respectively.[7] Therefore, the results demonstrated that HER followed a Volmer–Heyrovsky mechanism for Co@PC-7, whereas the Heyrovsky step was the rate-determining step.

The electrochemical active surface areas (ECSAs) of the studied electrocatalysts were estimated using double-layer capacitance ($C_{dl}$) values in a potential range of CV where the faradaic process does not occur (**Fig. 3C**). ECSA is proportional to the $C_{dl}$ values and to the number of catalytic active sites of the electrocatalysts according to the equation: $ECSA = C_{dl}/Cs$, where $C_s$ is a constant and also known as the specific capacitance and the $C_s$ value in an acidic solution is reported to be 0.035 $mF \cdot cm^{-2}$ for metal nanocatalysts.[27, 46] In this work, we also assumed a $C_s$ value of 0.035 $mF \cdot cm^{-2}$ according to previous studies.[46] Co@PC-7 has the largest $C_{dl}$ value (11.76 $mF \cdot cm^{-2}$) compared to the other electrocatalysts (1.06 $mF \cdot cm^{-2}$ for Co@PC-6 and 6.12 $mF \cdot cm^{-2}$ for Co@PC-8) (**Fig. 3D**). The corresponding ECSAs were then estimated to be 30.28, 336.0 and 174.85 $cm^2$ for the Co@PC-6, Co@PC-7 and Co@PC-8, respectively (**Table S5**). Co@PC-7, with the largest ECSA, will offer more catalytically active sites and, in turn, notably improve its electrocatalytic performance. The obtained current density normalized by ECSA is a suitable strategy to investigate the intrinsic catalytic performance of the electrocatalysts. HER polarization curves for Co@PC-6, Co@PC-7 and Co@PC-8 electrocatalysts normalized by their respective ECSAs are shown in **Fig. 3E**, with Co@PC-7 still displaying optimum HER performance after ECSA normalization. As proved via Raman spectroscopy, this specific temperature triggered the

formation of more edges and topological defects together with a larger surface area, which, in fact,

provided additional catalytic active sites in the surface of Co@PC-7 that markedly improve overall

electrocatalytic rates.[47] Turn over frequency (TOF) values are another key parameter which can

be calculated to investigate HER intrinsic activity of any electrocatalyst. TOF measures the

specific activity of the catalytic center for a specific reaction under the defined conditions from the

number of the catalytic cycles happening at the catalytic center per unit time.[26] The obtained TOF

values for Co@PC-6, Co@PC-7 and Co@PC-8 indicated the improved intrinsic catalytic activity

of Co@PC-7 at an applied overpotential of -0.3 V (**Table S3**). The current density normalized

TOF plot also demonstrated the superior activity of Co@PC-7 for HER (**Fig. 3F**). The mass

activity (MA) and specific activity (SA) at an overpotential of -0.3 V for Co@PC-6, Co@PC-7

and Co@PC-8 were then calculated and compared (**Fig. 3G** and **Table S3**). As for MA, Co@PC-7

was most active electrocatalyst for HER among all studied electrocatalysts, much higher than the

other catalysts as well as comparable to Pt/ C. Regarding SA, Co@PC-7 was also ~11 and 31 times

comparably more active to Co@PC-6 and Co@PC-8 electrocatalysts, respectively. The faradaic

efficiency of Co@PC-7 nanoparticles to produce molecular hydrogen was calculated by

comparing the moles of theoretically produced hydrogen with the experimental yields and the

obtained value was found to be 0.99 of 1 (**Fig. S6**). These findings confirmed the superior intrinsic

catalytic activity of Co@PC-7 nanoparticles, demonstrating the notable influence of the

carbonization temperature on HER overall rates. In this sense, the highly defective carbon porous

network obtained at 700°C provides charge redistribution at the metal/carbon electrochemical

interfaces giving rise to an interfacial charge polarization process in which the electrons are

collected at the catalytic surfaces (see XPS section). Importantly, Song and coworkers have been

previously demonstrated this phenomenon for CoP-defective carbon nanoparticles using

synchrotron-based X-ray absorption structure, ultraviolet photoelectron spectra (UPS), X-ray photoelectron spectroscopy (XPS) and density functional theory (DFT) calculations.[23] Undoubtedly, the electron gathering process at the defective interfacial carbons can efficiently regulate and tailor the electronic and surface properties of Co@PC-7, facilitating the electron transfer at the metal/carbon electrochemical interfaces, which most likely optimize adsorption energies of catalytic steps, thus boosting HER activity.[48, 49]

The durability of Co@PC-7 electrocatalyst was tested for HER by performing 1000 CV cycles at a scan rate of 50 mV·s$^{-1}$ between 0 and −0.8 V (vs RHE). After the 1000th cycle, the obtained LSV polarization curve was fitted with the initial LSV polarization curve to check the durability of the catalyst (**Fig. 3H**). It was found that the change in the current density was negligible, indicating the highly durable nature of Co@PC-7. Chronoamperometric measurements were also performed to further verify the stability of Co@PC-7 for 20,000 s. Remarkably, the electrocatalyst retained ~96% of current density even after ~20000 s, exhibiting remarkable long-term stability properties and predating the performance of state-of-the-art HER Pt/C electrocatalyst (**Fig. 3I**). Besides, the catalytic nanostructures exhibited remarkable long-term stability performance even for longer period of times (11.2 h), which can be attributed to the protection of the metal cores by the porous carbon matrix (**Fig. S8A**). We have further investigated the Co 2p XPS band of the Co@PC-7 catalyst after the chronoamperometric measurements to evaluate its structural integrity and no significant structural changes were observed on the catalytic surface (**Fig. S9**).

### 3.3 Electrochemical oxygen generation

The generation of molecular oxygen through the electrocatalytic water dissociation process represents a sustainable and green route as compared to conventional methods.[46] The electrocatalytic activity for OER process was investigated using a three-electrode system by carrying out LSVs of Co@PC-6, Co@PC-7, Co@PC-8 and commercial $RuO_2$ electrocatalysts in 0.1 M KOH solution at 2 mV·s$^{-1}$ (**Fig. 4A**). Among all studied catalysts, Co@PC-7 exhibited the most efficient OER activity, delivering an overpotential of 318 mV to achieve a current density of 10 mA·cm$^{-2}$ ($\eta_{10}$), whereas Co@PC-6, Co@PC-8 and commercial $RuO_2$ required an overpotential of 520, 430 and 327 mV, respectively, to obtain the same current density (**Table S3**). These findings suggested that OER electrocatalytic performance could be finely tuned by carbonization temperature. Therefore, the carbonization temperature is optimizing several key structural properties of Co@PC-7 such as surface area, number of defects on the carbon matrix and polarization charge distribution at the electrochemical interfaces, thus improving their catalytic activity. The viability and efficiency of Co@PC-7 nanoparticles were also comparable in terms of onset potential and $\eta_{10}$ with recent high-performance OER electrocatalysts (**Table S7**).

Strikingly, Co@PC-7 also outperformed by far the performance of the state-of-the-art OER electrocatalysts reported up to now in the literature such as $RuO_2$ ($\eta_{10}$ = 370 mV), $IrO_2$ ($\eta_{10}$ = 340 mV), $RuO_2$ NPs ($\eta_{10}$ = 460 mV) and Pt/C ($\eta_{10}$ = 629 mV) (**Fig. 4B** and **Table S7**). To gain more insight on the OER kinetics, Tafel plots were obtained from the LSV scans for all electrocatalysts and inspected. The calculated Tafel slope values were found to be 250, 80, 147 and 92 mV·dec$^{-1}$ for Co@PC-6, Co@PC-7, Co@PC-8 and $RuO_2$, respectively (**Fig. 4C**).
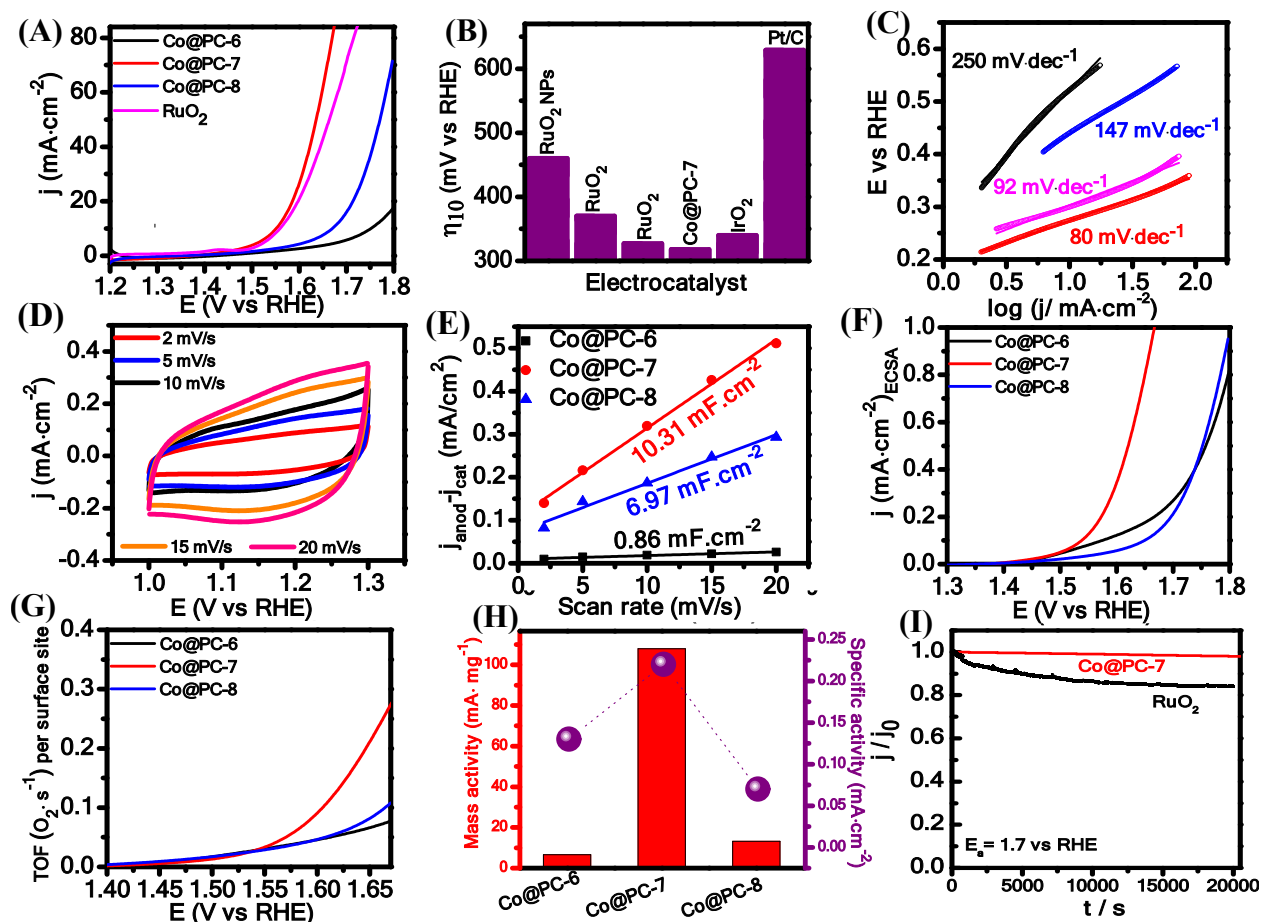
**Fig. 4** A) OER polarization curves and (C) the corresponding Tafel plots of Co@PC-6, Co@PC-7, Co@PC-8 and commercial $RuO_2$ in 0.1 M KOH solution at 2 mV·s$^{-1}$; (B) $\eta_{10}$ values for Co@PC-7 and the benchmarks $RuO_2$, $IrO_2$ and Pt/C electrocatalysts; (D) electrochemical capacitance measurements to determine the ECSA of Co@PC-7 at OER condition; E) plots of the difference of anodic and cathodic current densities against the scan rate for Co@PC-6, Co@PC-7 and Co@PC-8 catalysts; (F) OER polarization curves normalized by ECSA; (G) the average turn-over frequencies ($TOF_{avg}$) of the nanocatalysts in (A) per surface site; (H) mass and specific activity values of Co@PC-6, Co@PC-7 and Co@PC-8 catalysts; (I) I-t curves of Co@PC-7 electrocatalyst and its comparison with commercial $RuO_2$ at 1.70 V vs RHE.

The Co@PC-7 catalyst exhibited a much lower Tafel slope than those of the other cobalt-based catalysts and even lower than the benchmark $RuO_2$, demonstrating an excellent kinetic for the OER process.

It is well-known that the oxygen evolution or electrochemical oxidation of water usually occurs on a surface hydroxide/oxide layer.[50] When the metal is dipped in an alkaline solution, an adsorbed hydroxide layer is formed spontaneously on the metal surface. The most widely accepted OER mechanism was proposed by Otagawa and Bockris.[50] In this mechanism, the first step includes the adsorption of hydroxide ions and subsequently, their discharge to generate an adsorbed hydroxide layer on the metal surface under the oxidizing conditions, as seen in eq. (7). In the following step, the adsorbed hydroxide reacts with hydroxide ions to generate an oxide layer along with the release of an electron and a water molecule eq. (8). Afterward, a hydroxylation reaction takes place which involves the reaction between the oxide layer and hydroxide ions to form an oxide-hydroxide layer ($OOH^*$ species) as given in eq. (9). Then the $OOH^*$ species undergo a reaction with hydroxide ions to generate adsorbed oxygen and water with the subsequent release of one electron eq. (10). The final step involves the desorption of oxygen (eq. 11).

$$M + OH^- \longrightarrow MOH^* + e^- \tag{7}$$

$$MOH + OH^- \longrightarrow MO^* + H_2O + e^- \tag{8}$$

$$MO + OH^- \longrightarrow MOOH^* + e^- \tag{9}$$

$$MOOH + OH^- \longrightarrow MO_2 + H_2O + e^- \tag{10}$$

$$MO_2 \longrightarrow M + O_2 \tag{11}$$

DFT calculations have determined that the most critical step in the water oxidation process is the generation of (OOH*)-type species, which are the key intermediates catalytic species.[31] The adsorption of OOH* intermediate catalytic species can be nicely tailored by the interfacial polarization processes at the metal/C interfaces.[45,51] In this direction, the "electron gathering effect", which is taking places at the carbon/metal interfaces can give rise to the accumulation of holes at the metallic surface cores that can act like highly active ORR sites, thus decreasing the uphill energy state for the generation of OOH* species.[52]

To get a better understanding on the reason behind the superior activity of Co@PC-7, the ECSA of the prepared electrocatalysts was evaluated under OER conditions through determining the double-layer capacitance ($C_{dl}$). The cyclic voltammograms (CV) of the electrocatalysts were measured at different scan rates (2, 5, 10, 15 and 20 mV·s$^{-1}$) from 1.0 to 1.3 V vs. RHE considering the non-faradaic zone of the CV curve (**Fig. 4D**) and the difference between the anodic and cathodic currents is plotted against the scan rates to obtain the $C_{dl}$ values. The $C_{dl}$ values were found to be 0.86, 10.31 and 6.97 mF·cm$^{-2}$ for Co@PC-6, Co@PC-7 and Co@PC-8, respectively (**Fig. 4E**). Considering the specific capacitance ($C_s$) of about 0.04 mF·cm$^{-2}$ in this study, based on the fact that the $C_s$ values are normally reported to be in the range of 0.022-0.130 mF·cm$^{-2}$ in the alkaline solution, the ECSAs was calculated to be 21.5, 257.75 and 174.25 cm$^2$ for the Co@PC-6, Co@PC-7 and Co@PC-8 electrocatalysts, respectively (**Table S5**).[26] It must be noted that the obtained ECSA of Co@PC-7 is higher than that of many other recent OER electrocatalysts,[26] as well as higher than those of Co@PC-6 and Co@PC-8 electrocatalysts, indicating the presence of higher electroactive sites on its surface. Interestingly, even after the normalization of the current density to ECSA, the Co@PC-7 displayed the superior OER activity (**Fig. 4F**).

TOF, mass activity (MA) and specific activity (SA) parameters were calculated to have a further deeper look at the intrinsic properties of the prepared electrocatalysts for the OER process and the results are tabulated in **Table S3**. The TOF value of Co@PC-7 was found to be 47.88 s$^{-1}$ which is much higher than those of the Co@PC-6 (2.96 s$^{-1}$) and Co@PC-8 (5.91 s$^{-1}$) electrocatalysts, indicating a substantial enhancement of the intrinsic catalytic activity of Co@PC-7 at an applied overpotential of 1.65 V vs. RHE. The current density normalized TOF plot also displayed the best performance of Co@PC-7 electrocatalyst (**Fig. 4G**). The calculated MA value of Co@PC-7 (107.97 mA·mg$^{-1}$) was found to be ~16 and 8 times higher than that of Co@PC-6 (6.61 mA·mg$^{-1}$) and Co@PC-8 (13.27 mA·mg$^{-1}$), respectively. Furthermore, the SA of Co@PC-7 (0.22 mA·cm$^{-2}$) was found to be ~1.70 and 3.14 times higher than the Co@PC-6 (0.13 mA·cm$^{-2}$) and Co@PC-8 (0.07 mA·cm$^{-2}$), respectively (**Fig. 4H**). The faraday efficiency was calculated to be very close to 1 (0.98), thus confirming the excellent electrocatalytic activity of the Co@PC-7 electrocatalyst (**Fig. S10**).

The durability of Co@PC-7 catalyst towards the OER process was investigated by carrying out the cyclic voltammetry measurements at a scan rate of 50 mV·s$^{-1}$ for 1000 cycles. Afterward, the LSV scan of the catalyst was performed after 1000 cycles and compared with the initial LSV scan. It was observed only a slight change in the obtained current density, indicating the highly durable nature of Co@PC-7 (**Fig. S7**). Furthermore, Co@PC-7 displayed outstanding stability for OER with respect to RuO$_2$. **Fig. 2I** illustrates only about 2% reduction of the current density for Co@PC-7 after a 20 000 s chronoamperometric measurement with the continuous flow of the oxygen into the 0.1 M KOH solution. However, the RuO$_2$ catalyst lost 15% of its initial performance under the same reaction conditions, demonstrating the higher OER long-term stability

of Co@PC-7. Furthermore, the nanocatalysts also showed excellent electrochemical stability properties at longer times (11.2 h) (**Fig. S8B**).

### 3.4 Electrochemical oxygen reduction

ORR activity of Co@PC-6, Co@PC-7 and Co@PC-8 electrocatalysts was also evaluated using a conventional three-electrode system in $O_2$ saturated 0.1 M KOH solution under static and dynamic regimes. As seen in **Fig. 5A**, typical oxygen reduction peaks were observed at around 0.63, 0.72, and 0.64 V (vs RHE) for Co@PC-6, Co@PC-7 and Co@PC-8 catalysts, respectively, demonstrating the higher activity of Co@PC-7 for the oxygen electroreduction process. Under static conditions, Co@PC-7 exhibited the most competitive ORR performance rendering a Pt-like onset potential of 0.946 V vs RHE and a half-wave potential of 0.86 V vs RHE, which largely outperformed the values of Co@PC-6 ($E_{onset}$ = 0.785 V, $E_{1/2}$ = 0.64 V) and Co@PC-8 ($E_{onset}$ = 0.873 V, $E_{1/2}$ = 0.77 V) and close to Pt/C values ($E_{onset}$ = 0.987 V, $E_{1/2}$ = 0.89 V). Notably, the catalytic activity of Co@PC-7 was comparable and even better with other top-tier carbon-encapsulated catalysts including Co@NC/rGO ($E_{onset}$ = 0.98 V, $E_{1/2}$ = 0.86 V), Fe–N–C-800 ($E_{onset}$ = 0.97 V, $E_{1/2}$ = 0.88 V) and Co−Ni NOF ($E_{onset}$ = 0.96 V, $E_{1/2}$ = 0.88 V (**Table S8**).

To get a deeper understanding on ORR kinetics, Tafel plots were obtained from LSV experiments and the corresponding Tafel slopes were then calculated, as shown in **Fig. 5C**. Co@PC-7 electrocatalyst exhibited the lowest Tafel slope (94 mV·dec$^{-1}$), indicating a superior kinetic efficiency in OER processes at the Co metal/carbon catalytic interfaces. To obtain insightful knowledge on the dynamic ORR behavior of Co@PC-7 nanocatalyst, rotating-disk voltammetry (RDV) measurements were successfully accomplished at different rotation rates, between 250 and 2500 rpm, in 0.1 M KOH solution at a scan rate of 10 mV·s$^{-1}$ (**Fig. 5D**).
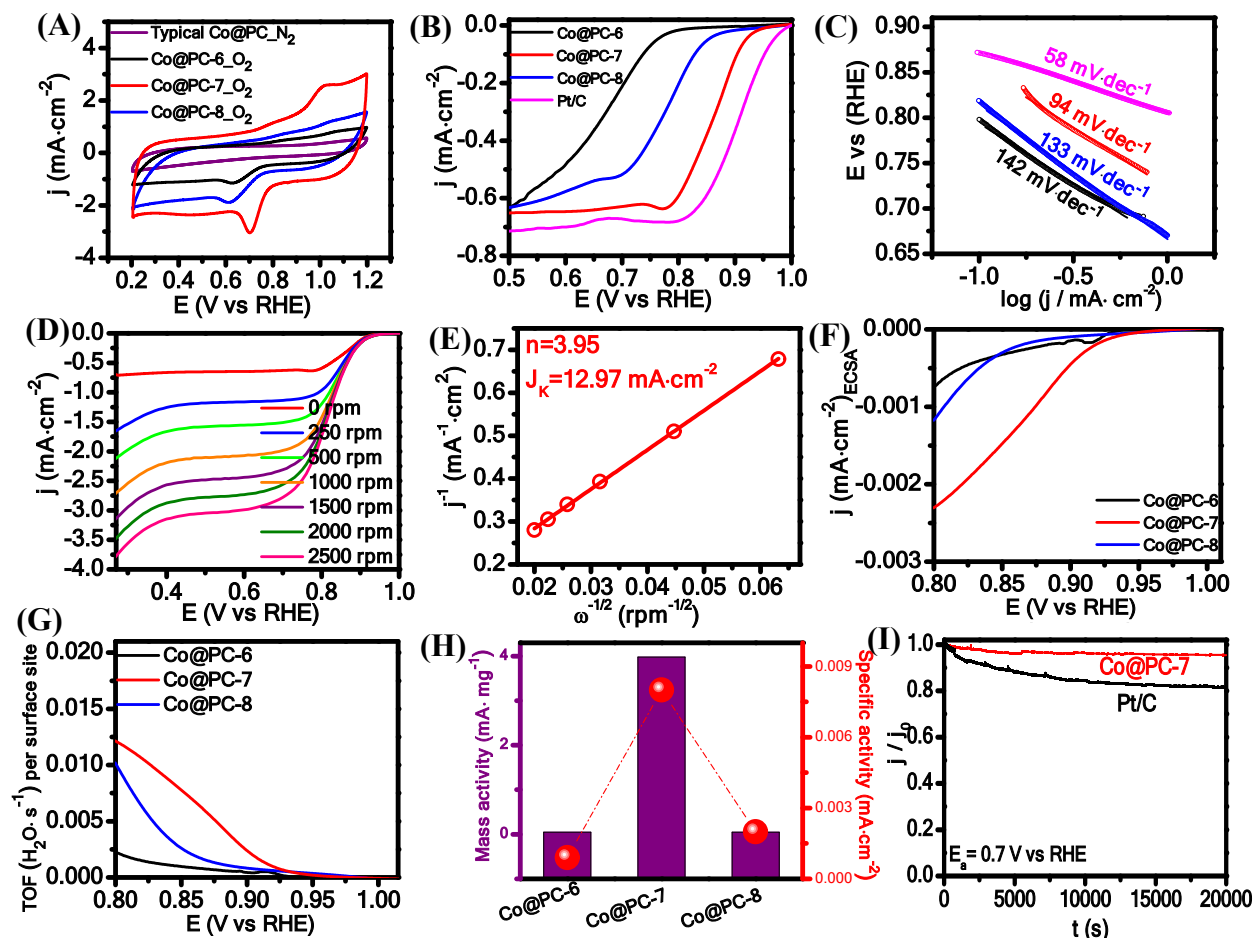
**Fig. 5** A) CVs of the Co@PC-6, Co@PC-7 and Co@PC-8 electrocatalysts in $N_2$ and $O_2$-saturated 0.1 M KOH solutions at 50 mV·s$^{-1}$; B) LSVs for ORR of Co@PC-6, Co@PC-7, Co@PC-8 and commercial Pt/C in 0.1 M KOH at 2 mV·s$^{-1}$ and C) the corresponding Tafel plots; D) rotating disk voltammogram (RDVs) curves at different rotation rates for Co@PC-7; E) the corresponding K-L plots; F) OER polarization curves normalized by ECSA; G) the average turn-over frequencies (TOF$_{avg}$) of the nanocatalysts displayed in (B) per surface site; H) mass and specific activity values of the Co@PC-6, Co@PC-7 and Co@PC-8 electrocatalysts; I) I-t curves of Co@PC-7 electrocatalyst and its comparison with commercial Pt/C at 0.7 V vs RHE.

The dynamic ORR onset potential was found to be 0.95 V vs RHE, which is in good agreement with the onset potential value measured in static conditions indicating that the dynamic conditions are not affecting the onset of the catalytic process. K-L plot for Co@PC-7 is shown in **Fig. 5E**. The excellent linear fitting demonstrates a first-order reaction toward dissolved $O_2$.[53] From K-L equations, the average number of electrons transferred (n) per oxygen molecule at 0.6 V vs RHE and the resulting kinetic-limiting current density ($J_k$) values were estimated to be 3.95 and 12.97 mA·cm$^{-2}$, respectively. It is worth noting that the number of electrons exchanged per $O_2$ molecule is close to 4 in Co@PC-7 active sites, indicating that the reaction is mainly following the most efficient four-electron-pathway.

The obtained electrochemically active surface area under OER conditions was taken into consideration in the ORR process as both OER and ORR processes were performed in the same experimental conditions. Co@PC-7 displayed much higher ECSA than others, thereby delivering more active sites to enhance the ORR performance. Furthermore, the current density was also normalized by the ECSA and it was observed that Co@PC-7 still provided optimum ORR performance (**Fig. 5F**). Additionally, several key parameters of the nanocatalysts such as TOF, mass activity (MA) and specific activity (SA) were also calculated to obtain in-depth information about the intrinsic catalytic activity of the electrocatalysts and the results are shown in **Table S4**. In catalysis, the best figure of merit to compare intrinsic activities among different materials is the TOF number, which gives a measure of the number of water molecules evolved per second per active site from the ORR process. In this direction, it is worth noting that the number of generated water molecules on Co@PC-7 catalytic surface fairly surpassed the other two electrocatalysts yields at a wide potential range of 0.80-0.90 V vs RHE, revealing that the catalytic performance of Co@PC-7 is even more efficient at the subnanometer level, where each tiny active site is able

to produce more water molecules in a very high potential window (**Fig. 5G**). This behavior was also confirmed by the MA and SA trends (**Fig. 5H**). The superior catalytic yields of Co@PC-7 can be ascribed to different factors that were introduced in previous sections: (i) the larger electrochemical surface area and (ii) the interfacial charge redistribution, which substantially modify the adsorption energy states of the intermediate catalytic steps favoring the oxygen reduction rates. The chronoamperometric measurements of Co@PC-7 and Pt/C electrocatalysts were also carried out and it was found that Co@PC-7 outperformed commercial ORR electrocatalyst (Pt/C) in terms of long-term stability properties, maintaining the 97% of the initial current applied after 20000s (**Fig. 5I**). Additionally, the nanocatalysts kept rendering an excellent electrochemical stability behavior at longer times (**Fig. S8C**).

**Table 1.** Comparison of bifunctional performance of Co@PC-7 with state-of-the-art bifunctional electrocatalysts under alkaline condition.

| Sample | $\eta_{10}$ (V) | $E_{1/2}$ (V) | $\Delta E$ (V) | Reference |
|---|---|---|---|---|
| Co-NC@Al$_2$O$_3$ | 1.65 | 0.86 | 0.79 | 54 |
| CoFe/Co@NCNT/NG | 1.61 | 0.87 | 0.74 | 55 |
| NiFe-LDH/Co,N-CNF | 1.54 | 0.79 | 0.75 | 56 |
| NiO/CoN PINWs | 1.53 | 0.68 | 0.85 | 57 |
| rGO/(Ni$^{2+}$/THPP/Co$^{2+}$/THPP)$_8$ | 1.56 | 0.70 | 0.86 | 58 |
| TA-NiFe@NCNT | 1.56 | 0.81 | 0.75 | 59 |
| Co@PC-7 | 1.55 | 0.86 | 0.69 | This work |

In order to evaluate the efficiency of the bifunctional catalytic performance of Co@PC-7 catalyst, the potential difference ($\Delta E$) between the overpotential at 10 mA·cm$^{-2}$ of OER and the half-wave potential of ORR, which is an effective descriptor for the overall oxygen activity, was calculated (**Table 1**). The potential difference ($\eta_{10}$-$E_{1/2}$) parameter for Co@PC-7 was estimated to be 0.68 V, indicating an ultra-reversible bifunctional ORR/OER catalytic process, which outperforms the values obtained for the majority of the state-of-the-art bifunctional catalyst under alkaline conditions.

### 3.5 Insights on the superior trifunctional electrocatalytic activity of Co@PC-7

To gain a deeper understanding of the remarkable trifunctional electrocatalytic activity of Co@PC-7 nanocatalyst, we further thoroughly analyzed the BET results. This study clearly demonstrated the mesoporous structure of Co@PC-7 catalyst with a higher surface area and an average pore size of 3.85 nm (**Fig. 1H**). On the other hand, the other two Co@PC-6 and Co@PC-8 electrocatalysts displayed a lower surface area of about 65 and 41 m$^2$·g$^{-1}$, respectively (**Fig. S11A**). Especially, the BJH pore size distribution plot of Co@PC-8 showed a narrow size distribution centered at 8.43 nm as well as a broad size distribution ranging from ~10 to 20 nm (**Fig. S11C**). The larger mesopore sizes of Co@PC-8 is provoked for the particle agglomeration processes that occur at higher temperatures, which facilitate the formation of interparticular pores, thus decreasing the surface area of Co@PC-8, as evidenced by the TEM analysis (**Fig. 2G**). Apparently, the high BET surface area is mainly ascribed to the mesoporous structure. As a result, the higher surface area of Co@PC-7 can offer a larger surface density of electrocatalytically available active sites that are exposed to the HER, OER and ORR-relevant species (H$^*$, H$_2$O, O$_2$, OH$^-$) and the mesoporous structure can also deliver the possibility of effective mass transport leading to the improved catalytic activity.[7] Furthermore, the electrocatalytic performance of Co@PC-8 was

higher than Co@PC-6 despite its smaller BET surface area. Therefore, the improvement in the electrocatalytic activity of Co@PC-8 can't be described in terms of BET surface area. The electrical conductivity of amorphous materials is usually less than their crystalline counterparts as well as the higher crystalline materials posse higher conductivity. We assume that the sintering method instigated by the pyrolysis did not only result in particle aggregation but also result in improved electrical conductivity. This improved electrical conductivity can enhance the charge transfer process in Co@PC-8 due to higher crystallinity and that should have contributed mostly to the observed pronounced electrocatalytic activity than Co@PC-6.
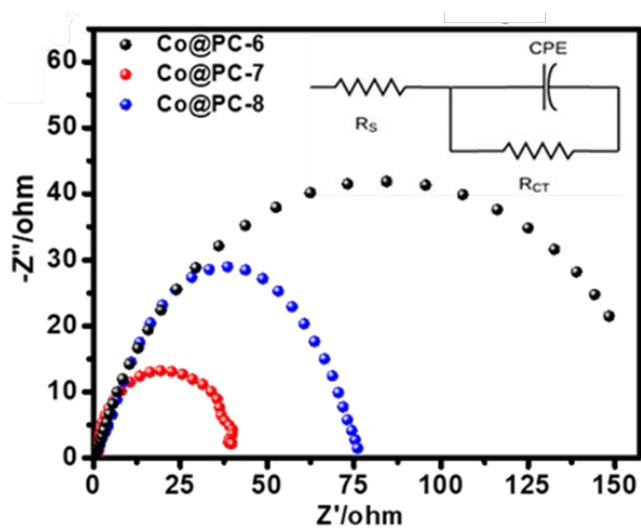


**Fig. 6** Nyquist plots of the Co@PC-6, Co@PC-7 and Co@PC-8 electrocatalysts for HER (inset: the circuit module that was applied to fit the corresponding Nyquist plots).

To support the obtained results from BET analysis, electrochemical impedance spectroscopy (EIS) experiments were further carried out to evaluate the charge transfer properties of the Co@PC electrocatalysts, which could be described by Nyquist plots (**Fig. 6**) and an equal circuit (**Fig. 6: inset**), where $R_s$ is the ohm resistance, $R_{ct}$ is the charge transfer resistance derived from the HER process and CPE is the constant phase element. The capacitive semicircles that are present in the

Nyquist plots for all catalysts confirmed that the electrocatalytic HER process is dynamically controlled. The obtained charge-transfer resistance of Co@PC-7 ($R_{CT}$ = 31.71 $\Omega$) was found to be 2.21 and 3.66 times lower than that of Co@PC-8 ($R_{CT}$ = 70.15 $\Omega$) and Co@PC-6 ($R_{CT}$ = 115.92 $\Omega$), respectively. The lower charge transfer resistance is correlated with the superior charge transport properties at the catalytic surface of Co@PC-7, which markedly facilitates the charge migration from the electrode surfaces to the electrochemical active sites, thus boosting the overall HER activity.[60]

Further, to investigate the individual contributions of porous carbon (PC) and cobalt nanoparticles on the electrocatalytic performance of Co@PC-7, we have tested them as HER electrocatalysts and compared their performance to Co@PC-7 (**Fig. S12**). As seen, both of them (unsupported Co NPs and PC) exhibited poor performance, whereas, Co@PC-7 displayed significantly higher performance for HER process. These results demonstrated that the improved activity of Co@PC-7 nanohybrid composite is mainly due to the collective action of PC and cobalt nanoparticles in the composite as a whole and it can then be assumed that there is a synergistic effect between the PC and cobalt nanoparticles in Co@PC-7. Hence, apart from the smaller charge transfer resistance, electron gathering process, higher BET as well as electrochemically active surface area, the excellent synergistic interaction between the PC and cobalt nanoparticles in Co@PC-7 nanohybrid also plays a vital role in boosting the trifunctional electrocatalytic performance of Co@PC-7.

## 4. Conclusions

A one-pot carbothermal reduction methodology was used as a sustainable strategy to fabricate porous carbon-embedded cobalt nanoparticles as highly active trifunctional electrocatalysts for OER/HER/ORR reactions. The structural properties of as-synthesized

nanocatalysts as well as their trifunctional catalytic activity were nicely tuned by the carbonization temperature. Importantly, the impressive multifunctional electrocatalytic activity of Co@PC-7 was directly correlated to their unique structural properties, which promote the interfacial charge polarization processes at the electrochemical interfaces providing highly active catalytic sites and, thus improving the trifunctional water splitting electrocatalysis. In summary, this study offers an eco-friendly and simple route for the green synthesis of carbon-encapsulated Co nanoparticles as non-precious state-of-the-art trifunctional electrocatalysts with remarkable multifunctional electrocatalytic properties.

**Conflicts of interest**

There are no conflicts to declare.

**Acknowledgments**

**References**

1.　　S. Chu, Y. Cui and N. Liu, *Nat. Mater.*, 2017, **16**, 16-22.

2.　　W. Li, Z.-Y. Hu, Z. Zhang, P. Wei, J. Zhang, Z. Pu, J. Zhu, D. He, S. Mu and G. Van Tendeloo, *J.Catal.*, 2019, **375**, 164-170.
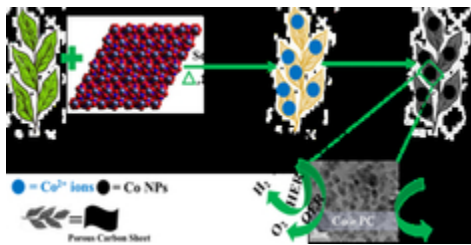
3.  D. Rodriguez-Padron, M. A. Ahsan, M. F. Sanad, R. Luque and A. R. P. Santiago, *Top. Curr. Chem.,* 2020, **378**, 1-19.

4.  S. Iravani and R. S. Varma, *Green Chem.*, 2020, **22**, 2643-2661.

5.  N. G. García-Peña, R. Redón, A. Herrera-Gomez, A. L. Fernández-Osorio, M. Bravo-Sanchez and G. Gomez-Sosa, *Appl. Surf. Sci.*, 2015, **340**, 25-34.

6.  M. A. Ahsan, V. Jabbari, A. A. El-Gendy, M. L. Curry and J. C. Noveron, *Appl. Surf. Sci.*, 2019, **497**, 143608.

7.  Z. Chen, R. Wu, Y. Liu, Y. Ha, Y. Guo, D. Sun, M. Liu and F. Fang, *Adv. Mater.*, 2018, **30**, 1802011.

8.  R. Ding, Q. Chen, Q. Luo, L. Zhou, Y. Wang, Y. Zhang and G. Fan, *Green Chem.*, 2020, **22**, 835-842.

9.  S. G. Peera, J. Balamurugan, N. H. Kim and J. H. Lee, *Small*, 2018, **14**, 1800441.

10. L. Zeng, X. Li, S. Fan, J. Mu, M. Qin, X. Wang, G. Gan, M. Tadé and S. Liu, *ACS Sustain. Chem. Eng.*, 2019, **7**, 5057-5064.

11. B. Weng, X. Wang, C. R. Grice, F. Xu and Y. Yan, *J. Mater. Chem. A*, 2019, **7**, 7168-7178.

12. J. Ding, S. Ji, H. Wang, H. Gai, F. Liu, B. G. Pollet and R. Wang, *Chem. Commun.*, 2019, **55**, 2924-2927.

13. H. Sun, Z. Yan, F. Liu, W. Xu, F. Cheng and J. Chen, *Adv. Mater.*, 2020, **32**, 1806326.

14. W. Wan, S. Wei, J. Li, C. A. Triana, Y. Zhou and G. R. Patzke, *J. Mater. Chem. A*, 2019, **7**, 15145-15155.

15. C. Huang, W. Fan and X. Qiu, *Sci. Rep.*, 2015, **5**, 16736.

16. C. Levard, E. M. Hotze, G. V. Lowry and G. E. Brown Jr, *Environ. Sci. Technol*, 2012, **46**, 6900-6914.

17.     K. Maeda, K. Teramura, D. Lu, N. Saito, Y. Inoue and K. Domen, *Angew. Chem.*, 2006, **118**, 7970-7973.

18.     S. Wu, W. Sun, J. Chen, J. Zhao, Q. Cao, W. Fang and Q. Zhao, *J. Catal.*, 2019, **377**, 110-121.

19.     D. K. Yoon, A. Kumar, D.-G. Lee, J. Lee, T. Kwon, J. Choi, T. Jin, J. H. Shim and I. S. Lee, *Nano Lett.*, 2019, **19**, 3627-3633.

20.     H. Khani, N. S. Grundish, D. O. Wipf and J. B. Goodenough, *Adv. Energy Mater.*, 2020, **10**, 1903215.

21.     N. Cheng, N. Wang, L. Ren, G. Casillas-Garcia, N. Liu, Y. Liu, X. Xu, W. Hao, S. X. Dou and Y. Du, *Carbon*, 2020, **163**, 178-185.

22.     S. Feng, L. Yang, Z. Zhang, Q. Li and D. Xu, *ACS Appl. Energy Mater.*, 2019, **3**, 943-950.

23.     Y. Lin, L. Yang, Y. Zhang, H. Jiang, Z. Xiao, C. Wu, G. Zhang, J. Jiang and L. Song, *Adv. Energy Mater.*, 2018, **8**, 1703623.

24.     M. G. Ferruzzi, *Physiology & behavior*, 2010, **100**, 33-41.

25.     P. Panneerselvam, N. Morad and K. A. Tan, *J. Hazard. Mater.*, 2011, **186**, 160-168.

26.     M. Sadaqat, L. Nisar, F. Hussain, M. N. Ashiq, A. Shah, M. F. Ehsan, M. Najam-Ul-Haq and K. S. Joya, *J. Mater. Chem. A*, 2019, **7**, 26410-26420.

27.     U. De Silva, J. Masud, N. Zhang, Y. Hong, W. P. Liyanage, M. A. Zaeem and M. Nath, *J. Mater. Chem. A*, 2018, **6**, 7608-7622.

28.     X. Liu, W. Yang, L. Chen, Z. Liu, L. Long, S. Wang, C. Liu, S. Dong and J. Jia, *ACS Appl. Mater. Interfaces*, 2020, **12**, 4463-4472.

29.     D. Rodriguez-Padron, A. R. Puente-Santiago, M. Cano, A. Caballero, M. J. Munoz-Batista and R. Luque, *ACS Appl. Mater. Interfaces*, 2019, **12**, 2207-2215.

30. L. Li, R. Jiang, W. Chu, H. Cang, H. Chen and J. Yan, *Catal. Sci. Technol.*, 2017, **7**, 1363-1371.

31. J. Masa, P. Weide, D. Peeters, I. Sinev, W. Xia, Z. Sun, C. Somsen, M. Muhler and W. Schuhmann, *Adv. Energy Mater.*, 2016, **6**, 1502313.

32. D. W. Wang, F. Li, M. Liu, G. Q. Lu and H. M. Cheng, *Angew. Chem. In. Ed.*, 2008, **47**, 373-376.

33. Y. Zhai, Y. Dou, X. Liu, S. S. Park, C.-S. Ha and D. Zhao, *Carbon*, 2011, **49**, 545-555.

34. M. A. Ahsan, A. R. Puente Santiago, Y. Hong, N. Zhang, M. Cano, E. Rodriguez-Castellon, L. Echegoyen, S. T. Sreenivasan and J. C. Noveron, *J. Am. Chem. Soc.*, 2020, **142**, 14688–14701.

35. Z. Li, W. Lv, C. Zhang, B. Li, F. Kang and Q.-H. Yang, *Carbon*, 2015, **92**, 11-14.

36. Y. Su, Y. Zhu, H. Jiang, J. Shen, X. Yang, W. Zou, J. Chen and C. Li, *Nanoscale*, 2014, **6**, 15080-15089.

37. K. Iris, X. Xiong, D. C. Tsang, L. Wang, A. J. Hunt, H. Song, J. Shang, Y. S. Ok and C. S. Poon, *Green Chem.*, 2019, **21**, 1267-1281.

38. Y. Su, H. Jiang, Y. Zhu, X. Yang, J. Shen, W. Zou, J. Chen and C. Li, *J. Mater. Chem. A*, 2014, **2**, 7281-7287.

39. I. Y. Jeon, S. Zhang, L. Zhang, H. J. Choi, J. M. Seo, Z. Xia, L. Dai and J. B. Baek, *Adv. Mater.*, 2013, **25**, 6138-6145.

40. M. Ibrahim, C. c. Marcelot-Garcia, K. Aït Atmane, E. Berrichi, L.-M. Lacroix, A. Zwick, B. Warot-Fonrose, S. Lachaize, P. Decorse and J.-Y. Piquemal, *J. Phys. Chem. C*, 2013, **117**, 15808-15816.

41.　　Z. D. Lei, Y. C. Xue, W. Q. Chen, L. Li, W. H. Qiu, Y. Zhang and L. Tang, *Small*, 2018, **14**, 1802045.

42.　　L. Li, J. Yan, T. Wang, Z.-J. Zhao, J. Zhang, J. Gong and N. Guan, *Nat. Commun.*, 2015, **6**, 1-10.

43.　　M. Chu, C. Chen, W. Guo, L. Lu, Y. Wu, H. Wu, M. He and B. Han, *Green Chem.*, 2019, **21**, 2589-2593.

44.　　Y. Xiao, C. Hu, L. Qu, C. Hu and M. Cao, *Chem. Eur. J.*, 2013, **19**, 14271-14278.

45.　　Y. Tan, C. Xu, G. Chen, X. Fang, N. Zheng and Q. Xie, *Adv. Funct. Mater.*, 2012, **22**, 4584-4591.

46.　　C. C. McCrory, S. Jung, J. C. Peters and T. F. Jaramillo, *J. Am. Chem. Soc.*, 2013, **135**, 16977-16987.

47.　　C. Xie, D. Yan, W. Chen, Y. Zou, R. Chen, S. Zang, Y. Wang, X. Yao and S. Wang, *Mater. Today*, 2019, **31**, 47-68.

48.　　H. Jiang, J. Gu, X. Zheng, M. Liu, X. Qiu, L. Wang, W. Li, Z. Chen, X. Ji and J. Li, *Energ. Environ. Sci.*, 2019, **12**, 322-333.

49.　　Y. Jia, L. Zhang, A. Du, G. Gao, J. Chen, X. Yan, C. L. Brown and X. Yao, *Adv. Mater.*, 2016, **28**, 9532-9538.

50.　　J. O. M. Bockris and T. Otagawa, *J. Phys. Chem.*, 2002, **87**, 2960-2971.

51.　　D. Liang, C. Lian, Q. Xu, M. Liu, H. Liu, H. Jiang and C. Li, *Appl. Catal. B: Environ.*, 2020, **268**, 118417.

52.　　Z. Li, Y. Zhang, Y. Feng, C. Q. Cheng, K. W. Qiu, C. K. Dong, H. Liu and X. W. Du, *Adv. Funct. Mater.*, 2019, **29**, 1903444.

53. Y. Jia, L. Zhang, G. Gao, H. Chen, B. Wang, J. Zhou, M. T. Soo, M. Hong, X. Yan and G. Qian, *Adv. Mater.*, 2017, **29**, 1700017.

54. G. Tuci, C. Zafferoni, A. Rossin, A. Milella, L. Luconi, M. Innocenti, L. Truong Phuoc, C. Duong-Viet, C. Pham-Huu and G. Giambastiani, *Chem. Mater.*, 2014, **26**, 3460-3470.

55. M. Wang, C.-L. Dong, Y.-C. Huang and S. Shen, *J. Catal.*, 2019, **371**, 262-269.

56. L. Zhu, D. Zheng, Z. Wang, X. Zheng, P. Fang, J. Zhu, M. Yu, Y. Tong and X. Lu, *Adv. Mater.*, 2018, **30**, 1805268.

57. P. Zhu, J. Gao and S. Liu, *J. Power Sources*, 2020, **449**, 227512.

58. Q. Wang, L. Shang, R. Shi, X. Zhang, Y. Zhao, G. I. Waterhouse, L. Z. Wu, C. H. Tung and T. Zhang, *Adv. Energy Mater.* 2017, **7**, 1700467.

59. J. Yin, Y. Li, F. Lv, Q. Fan, Y.-Q. Zhao, Q. Zhang, W. Wang, F. Cheng, P. Xi and S. Guo, *ACS Nano*, 2017, **11**, 2275-2283.

60. J. Sun, H. Yin, P. Liu, Y. Wang, X. Yao, Z. Tang and H. Zhao, *Chem. Sci.*, 2016, **7**, 5640-5646.

19x9mm (300 x 300 DPI)